P H Y S I C A L   R E V I E W   L E T T E R S

Singlet-Triplet Dispersion Reveals Additional Frustration in the Triangular-Lattice Dimer Compound Ba₃Mn₂O₈

M. B. Stone,[1] M. D. Lumsden,[1] S. Chang,[2] E. C. Samulon,[3] C. D. Batista,[4] and I. R. Fisher[3]

[1]*Neutron Scattering Science Division, Oak Ridge National Laboratory, Oak Ridge, Tennessee 37831, USA*
[2]*NIST Center for Neutron Research, Gaithersburg, Maryland 20899, USA*
[3]*Department of Applied Physics and Geballe Laboratory for Advanced Materials, Stanford University, California 94305, USA*
[4]*Theoretical Division, Los Alamos National Laboratory, Los Alamos, New Mexico, 87545 USA*
(Received 28 April 2008; published 9 June 2008)

We present single crystal inelastic neutron scattering measurements of the $S = 1$ dimerized quasi-two-dimensional antiferromagnet Ba₃Mn₂O₈. The singlet-triplet dispersion reveals nearest-neighbor and next-nearest-neighbor ferromagnetic interactions between adjacent bilayers that compete against each other. Although the interbilayer exchange is comparable to the intrabilayer exchange, this additional frustration reduces the effective coupling along the c axis and leads to a quasi-two-dimensional behavior. In addition, the obtained exchange values are able to reproduce the four critical fields in the phase diagram.

The presence of exotic ground states [1], excitations [2], and quantum phase transitions [3] in a growing number of available materials is making low-dimensional gapped frustrated quantum magnets especially topical. In some cases, the ability to tune the system Hamiltonian via external fields allows access to additional phases. For instance, the singlet-triplet gap in the spectrum can be closed via application of external magnetic fields [4,5]. The resulting quantum critical point (QCP) separates a low field disordered paramagnet from a high field ordered phase which to a good approximation can be considered a Bose-Einstein condensation of magnons [6,7].

The hexagonal antiferromagnetic bilayer Ba₃Mn₂O₈ is established as a quasi-two-dimensional (2D) frustrated antiferromagnet with a quantum critical phase diagram [8,9]. Rather than a single Bose-Einstein condensate phase as in $S = \frac{1}{2}$ singlet-triplet antiferromagnets, Ba₃Mn₂O₈ has two sequential magnetically ordered phases, i.e., four zero-temperature QCPs, as a function of applied magnetic field: $\mu_0 H_{c1} \approx 9$ T, $\mu_0 H_{c2} \approx 26$ T, $\mu_0 H_{c3} \approx 32.3$ T, and $\mu_0 H_{c4} \approx 48$ T [10–12]. The first (second) ordered phase for $H_{c1} < H < H_{c2}$ ($H_{c3} < H < H_{c4}$) can be approximately described as singlet-triplet (triplet-quintet) condensation. The nature of these high field ordered phases fundamentally depends upon the zero-field exchange paths and constants.

Powder inelastic-neutron-scattering (INS) measurements of Ba₃Mn₂O₈ yielded three independent exchange constants through comparison to a spherically averaged scattering intensity [13]. The dimer exchange J_0 and interdimer exchanges are illustrated in Fig. 1(b). Examining these excitations using single crystal INS, we find next-nearest-neighbor (NNN) interactions J_4 play a significant and heretofore unexplored role in the propagation of triplet excitations in Ba₃Mn₂O₈. Since the dispersion bandwidth only depends on the difference $J_2 - J_3$, we determine the J_3 exchange by fitting the three measured critical fields

H_{c2}, H_{c3}, and H_{c4} simultaneously [10–12] (H_{c1} depends on the difference $J_2 - J_3$). We find that both interbilayer exchange constants, J_1 and J_4, are important in determining the critical fields. In addition, we show that although ferromagnetic, J_1 and J_4 are competing interactions due to the geometric frustration of the triangular bilayers and the interbilayer exchange paths. This explains why Ba₃Mn₂O₈ is a quasi-2D magnet in spite of the fact that the dominant interbilayer coupling J_1 is slightly larger than $|J_2 - J_3|$.

Single crystals of Ba₃Mn₂O₈ were grown from a flux melt as described in Ref. [9]. Five crystals with a net mass 0.372 g were coaligned using the HB1A triple-axis spectrometer (TAS) at the High Flux Isotope Reactor with a resulting mosaic of $\approx 42'$. INS measurements were performed on the SPINS cold neutron TAS at the NIST Center for Neutron Research. The instrument was configured with $80'$ collimation before the sample followed by a cooled Be filter and an $80'$ radial collimator. Measurements were performed with fixed final energy $E_f = 5$ meV selected by a 10.5 cm wide horizontally focusing analyzer. This configuration results in a measured elastic FWHM energy resolution at the $(0.3\ 0.3\ 3)$ wave vector of $\delta\hbar\omega = 0.294(7)$ meV. The majority of our data presented here consists of constant wave vector **Q** scans performed at $T = 1.7$ K in the (hhl) scattering plane.

Representative constant **Q** scans are shown in Fig. 1(a). The data show a single resolution limited mode propagating along the $(hh\frac{3}{2})$ direction between energy transfers $\hbar\omega$ of 1 and 3 meV. The bandwidth and gap of the spectrum are in good agreement with values determined from powder INS measurements [13]. Measurements at several high-symmetry locations in the $(hk0)$ scattering plane were also performed. These were made in the identical instrumental configuration with the focusing analyzer broadened to ≈ 23.1 cm to integrate over additional scattering intensity. The broadened line shape for $(\frac{1}{2}00)$ in Fig. 1(a) reflects the broadened Q resolution of the wider analyzer. As
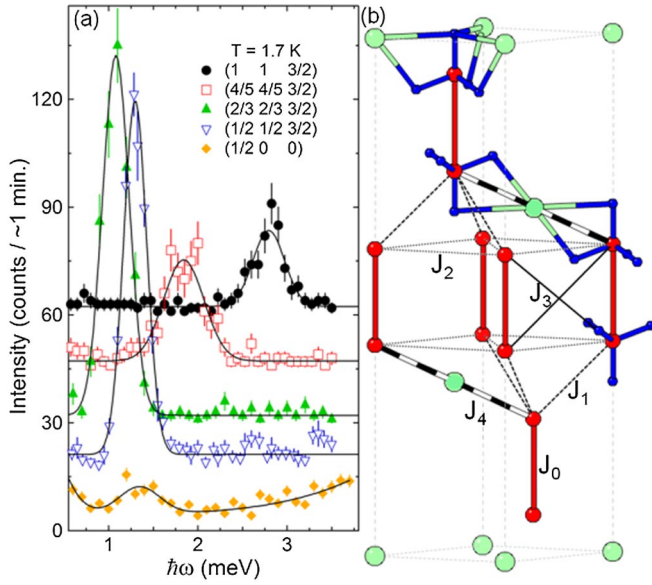
FIG. 1 (color online).   (a) Constant $\mathbf{Q}$ scans in the (hhl) and $(hk0)$ planes. Solid lines are Gaussian fits. The $(\frac{1}{2}00)$ fit includes a fixed elastic Gaussian and a higher energy Gaussian to account for incoherent elastic scattering and a scattering angle dependent background, respectively. Data are offset vertically for presentation. (b) Crystal structure of $Ba_3Mn_2O_8$ (c axis vertical) showing Mn^{5+} dimers (red dimer bonds along c axis) and 12-fold coordinated Ba sites (large green spheres) [23]. Oxygen sites (small blue spheres) involved in coordination of two dimers are shown to illustrate interdimer connectivity and tetrahedral coordination of the Mn^{5+}. Tenfold coordinated Ba sites are not shown for clarity. Exchange connectivity within and between $S = 1$ dimers is shown with different line types. J_3 is only shown for a single pair of dimers. Exchange constants correspond to Mn-Mn distances of 3.985 Å(J_0), 4.569 Å(J_1), 5.711 Å(J_2), 6.964 Å(J_3), and 7.313 Å(J_4).

shown in Fig. 1(a), the measured scattering intensity in the $(hk0)$ plane is very weak compared to the (hhl) plane.

To illustrate the dispersion and wave-vector dependent scattering intensity, we combine a series of constant $\mathbf{Q}$ scans in the image shown in Figs. 2(a)–2(d). Figure 2(i)

shows the path through wave-vector space for these data. Figure 2 indicates a single dispersive mode in both the $(hh\zeta)$ and $(\zeta\zeta l)$ directions. The dispersion along the $(hh\zeta)$ wave vectors has a distinct W shape with clear minima in the vicinity of $h \approx \frac{1}{3}$ and $h \approx \frac{2}{3}$ and a local maximum at the $h = \frac{1}{2}$. The dispersion along the l wave vector has a periodicity of three reciprocal lattice units (rlu).

One hundred twenty-six individual constant $\mathbf{Q}$ scans were separately fit to a single inelastic Gaussian peak. The peak positions along several high-symmetry directions are plotted in Figs. 2(a)–2(d) and along several $(\zeta\zeta l)$ wave vectors in Fig. 3(a). The singlet-triplet excitation is fairly dispersive along the $(00l)$ direction as shown in Fig. 2(d) and also along the l direction near the zone boundary as shown in Fig. 3(a) for $(0.15\ 0.15\ l)$. However, there is almost no dispersion along l for $0.3 \le h \le 0.7$. In fact for the $(\zeta\zeta l)$ scans shown in Fig. 3(a), the dispersion flattens and continuously changes phase as one moves from $\zeta = 0$ to $\zeta = \frac{1}{2}$.

The three original exchange constants determined from analysis of powder INS data do not account for the lack of dispersion along the l direction near the zone center. Rather we must include the NNN interbilayer interaction in the Heisenberg Hamiltonian J_4. As in the powder analysis, we use a dispersion based upon weakly coupled $S = 1$ dimers:

$$\hbar\,\omega^\nu(\mathbf{Q}) = \sqrt{\Delta_\nu^2 + \tfrac{8}{3}\Delta_\nu \mathcal{J}(\mathbf{Q})R(T)}, \qquad (1)$$

where $\nu = \{1, 0, -1\}$ denotes the spin projection S^z of the triplet excitation, $\mathcal{J}(\mathbf{Q})$ is the Fourier sum of interactions beyond dimer exchange, $\Delta_0 = J_0 + 2D/3$, $\Delta_{\pm1} = J_0 - D/3$, and $R(T)$ is the thermal population difference between ground and excited states. For $S = 1$ antiferromagnetic dimers,

$$R(T) = \frac{1 - \exp(-J_0\beta)}{1 + 3\exp(-J_0\beta) + 5\exp(-3J_0\beta)}, \qquad (2)$$

where $\beta = \frac{1}{k_B T}$. Including the J_4 interaction, the Fourier sum becomes

$$\omega_1 = \cos\!\left(\frac{2\pi}{3}[-h+k+l]\right) + \cos\!\left(\frac{2\pi}{3}[-h-2k+l]\right) + \cos\!\left(\frac{2\pi}{3}[2h+k+l]\right)$$

$$\omega_2 = \cos(2\pi k) + \cos(2\pi[h+k]) + \cos(2\pi h)$$

$$\omega_4 = \cos\!\left(\frac{2\pi}{3}[2h-2k+l]\right) + \cos\!\left(\frac{2\pi}{3}[2h+4k+l]\right) + \cos\!\left(\frac{2\pi}{3}[-4h-2k+l]\right)$$

$$\mathcal{J}(\mathbf{Q}) = J_1\omega_1 + 2(J_2 - J_3)\omega_2 + J_4\omega_4.$$

$$(3)$$

The small anisotropy $D = -0.032$ meV [9,13] has been determined from zero-field ESR experiments [14]. For $Ba_3Mn_2O_8$ in zero magnetic field, D will not change the dispersion and will only broaden the constant $\mathbf{Q}$ scans. As shown in Fig. 1(a), J_4 corresponds to NNN interdimer interactions along the c axis between bilayers. This exchange path is through the 12-fold coordinated Ba sites

which are coplaner with the O sites associated with the Mn tetrahedra. Each of the 12-fold coordinated Ba sites participates in three such J_4 exchange paths. A simultaneous fit of the peak positions of the constant $\mathbf{Q}$ scans in the (hhl) scattering plane yields $J_0 = 1.642(3)$, $J_1 = -0.118(2)$, $(J_2 - J_3) = 0.1136(7)$, and $J_4 = -0.037(2)$ meV. J_2 and J_3 represent interdimer exchange between the same spin
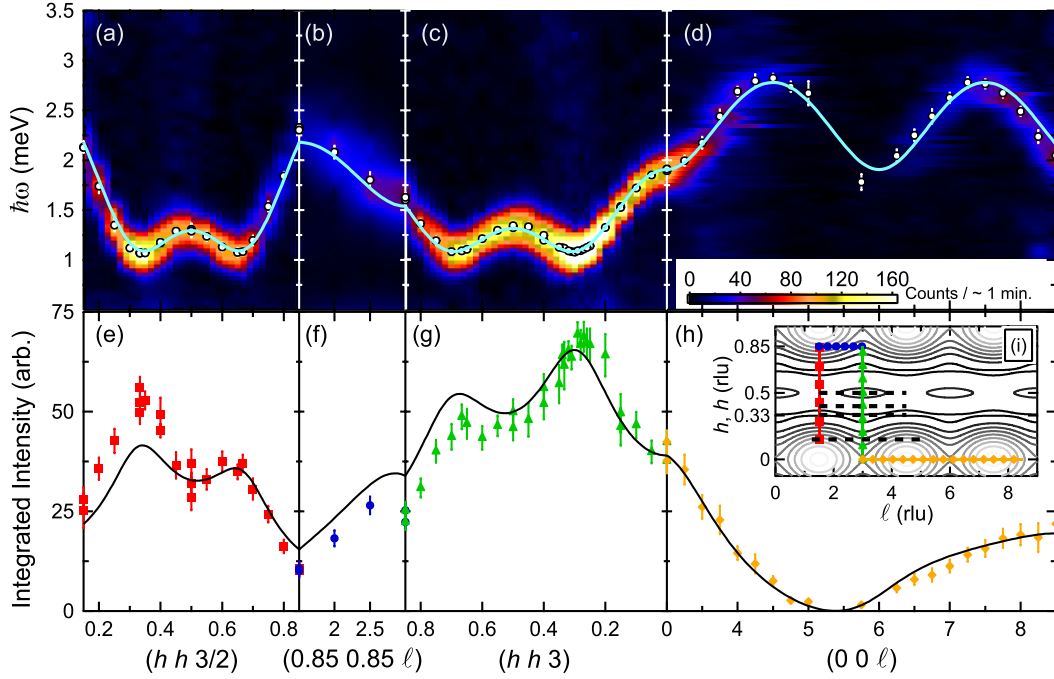
FIG. 2 (color online). (a)–(d) $T = 1.7$ K scattering intensity of $Ba_3Mn_2O_8$ vs $\hbar\omega$ and **Q**. Figure is interpolated from constant **Q** scans in the (hhl) plane. White circles are peak positions from Gaussian fits described in the text. Solid line is the fitted dispersion. (e)–(h) Integrated scattering intensity from Gaussian fits to constant **Q** scans. Solid line is the fitted scattering intensity. (i) Path through the (hhl) plane shown in (a)–(h). Dashed lines correspond to scans shown in Fig. 3. Contour lines are the fitted dispersion with dark (light) lines representing smaller (larger) energy transfers shown at 0.2 meV intervals. Horizontal axes of (a)–(h) are plotted in reciprocal lattice units (rlu).

dimers. They cannot be independently determined from the zero-field dispersion because $\mathcal{J}(\mathbf{Q})$ depends on their difference. The phase shift for triplets propagating between dimers via J_2 or J_3 [see Fig. 1(b)] is due to the opposite symmetries of the singlet (symmetric) and the triplet (antisymmetric) states under a permutation of the two sites that form the dimer. The corresponding dispersion curves shown in Figs. 2(a)–2(d) and 3(a) agree very well with the measurement. We also plot the fitted dispersion along $(\frac{1}{2} \frac{1}{2} l)$ for $J_4 = 0$ [dashed line in Fig. 3(a)]. It is clear that the NNN exchange is needed to describe the measured dispersion. The dispersion minimum $\hbar\omega = 1.081$ meV occurs at wave vectors $(\frac{1}{3} - \delta, \frac{1}{3} - \delta, l)$ and $(\frac{2}{3} + \delta, \frac{2}{3} + \delta, l)$ with $\delta \approx 0.0259$. This value is similar to that determined from our powder measurements, and recent mean-field calculations [12].

Figures 2(e)–2(h) and 3(b) show the **Q** dependent integrated scattering intensity. Based upon the established single mode approximation (SMA) dimer model [13], the magnetic scattering intensity for $k_B T \ll J_0$ is

$$I_m(\mathbf{Q}, \omega) \propto |F(Q)|^2 \frac{1 - \cos(\mathbf{Q} \cdot \mathbf{d})}{\hbar\omega(\mathbf{Q})} \delta(\hbar\omega - \hbar\omega(\mathbf{Q})), \quad (4)$$

where $|F(Q)|$ is the magnetic form factor [15,16] and **d** is the intradimer vector: $\mathbf{d} = 0.1858\mathbf{c}$. The dimer structure factor explains the lack of intensity found in the $(hk0)$ plane, i.e. $\mathbf{Q}_{(hk0)} \perp \mathbf{d}$. We fit the integrated intensity to

the SMA model in Eq. (4) using the dispersion found earlier and only a single multiplicative fitting parameter. The fit agrees quite well with the measured results. The dimer structure factor accounts for almost all of the scattering intensity.

The interdimer exchange corresponding to triplet propagation out of the hexagonal ab plane is ferromagnetic for both J_1 and J_4, whereas interdimer coupling in the hexagonal ab plane is entirely antiferromagnetic and consequently geometrically frustrated. We can gain insight into the consequences of the two interlayer couplings by considering the magnetic structure for $H_{c1} < H < H_{c2}$. The in-plane geometric frustration alone leads to a 120° magnetic structure for a single isolated bilayer. Such a structure blocks the interlayer couplings J_1 and J_4 because a spin $\mathbf{S}_i$ on a given bilayer interacts with the sum of three spins that are on the three different sublattices (A, B, and C) of the adjacent bilayer (this sum is zero for a 120° structure). Consequently, the ferromagnetic interaction J_1 induces a spiral phase ($\alpha \neq 120°$) [9,10] to have a net moment on each triangle. This moment is ferromagnetically coupled to the spin $\mathbf{S}_i$ that is at the center of the corresponding triangle (and in the next bilayer). However, such spiral distortion is not favorable for the ferromagnetic J_4 term: the three spins that are next-nearest-neighbors of $\mathbf{S}_i$ in the next bilayer form a bigger triangle and the net moment of this triangle is *antiferromagnetically* aligned with $\mathbf{S}_i$. Therefore, the J_1 exchange interaction competes against J_4 producing a
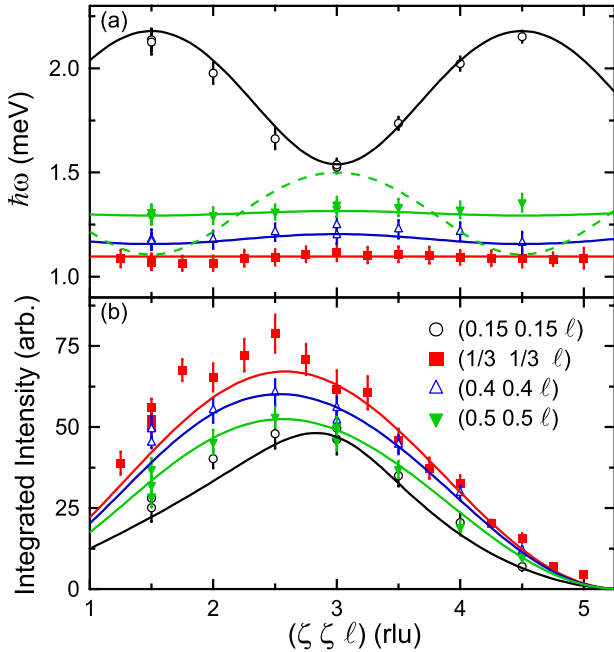
PHYSICAL REVIEW LETTERS

FIG. 3 (color online). (a) Dispersion and (b) integrated scattering intensity of $Ba_3Mn_2O_8$ determined from Gaussian fits to constant **Q** scans. Solid lines in (a) are fits to the dispersion as discussed in the text. Dashed line in (a) is the fitted dispersion for $(\frac{1}{2}\frac{1}{2}l)$ fixing $J_4 = 0$ resulting in exchange constants $J_0 = 1.640(8)$, $J_1 = -0.117(5)$, and $J_2 - J_3 = 0.109(2)$. Solid lines in (b) are fits to the scattering intensity as described in the text.

flatter singlet-triplet dispersion along the c axis, i.e., an effective quasi-2D-like behavior. This competition also leads to smaller deviation of α from 120°.

Based upon the determined exchange constants and an appropriate choice of $J_3 = 0.142$ meV ($J_2 = 0.256$ meV) we are able to reproduce the four measured critical fields to a good approximation. Using a two-level approach [10] keeping only the singlet ($S^z = 2$ quintet) and the $S^z = 1$ triplet dimer states for $H_{c1} < H < H_{c2}$ ($H_{c3} < H < H_{c4}$), we obtain values for the four critical fields: $\mu_0 H_{c1} = 10.24$ T, $\mu_0 H_{c2} = 26.44$ T, $\mu_0 H_{c3} = 33.25$ T, $\mu_0 H_{c4} = 47.5$ T using the measured value of $g = 2.01 \pm 0.03$. The agreement with the experimental values is quite good considering that neglecting the excited triplet $S^z = 0, -1$ states introduces errors of the order of 1 T. For instance, if we include the effect of quadratic fluctuations to the $S^z = 0, -1$ triplet states, the lowest critical field becomes $\mu_0 H_{c1} = \omega^1(\mathbf{Q}_{min})/g\mu_B = 9.34$ T in excellent agreement with the experimental value [$\mathbf{Q}_{min}$ is the wave vector that minimizes $\omega^1(\mathbf{Q})$].

Through single crystal INS measurements of $Ba_3Mn_2O_8$ we find that NNN exchange interactions are significant in describing the system. The nearest and NNN interbilayer couplings are both ferromagnetic. It is clear that the antiferromagnetic interactions within the bilayer lead to a geometrically frustrated system. However, for $Ba_3Mn_2O_8$ we find a novel case where ferromagnetic interbilayer

exchange actually serves to enhance the quasi-2D behavior of the bilayer. The refined exchange constants also provide a zero-field confirmation of the high magnetic field QCPs. In addition to marked progress in understanding the quantum critical phase diagram of $Ba_3Mn_2O_8$ and its excitations and ordered states, the determined dispersion should also be applicable to other isostructural gapped magnetic compounds in the $A_3Cr_2O_8$ series where $A = Ca^{2+}$, Sr^{2+}, or Ba^{2+} such as $Ba_3Cr_2O_8$ [17–20] and $Sr_3Cr_2O_8$ [21,22].

[1] K. C. Rule *et al.*, Phys. Rev. Lett. **100**, 117202 (2008); M. B. Stone *et al.*, Phys. Rev. Lett. **96**, 257203 (2006).
[2] H.-J. Mikeska and C. Luckmann, Phys. Rev. B **77**, 054405 (2008); B. D. Gaulin *et al.*, Phys. Rev. Lett. **93**, 267202 (2004).
[3] S. E. Sebastian *et al.*, Nature (London) **441**, 617 (2006); C. D. Batista *et al.*, Phys. Rev. Lett. **98**, 257201 (2007); J. Schmalian and C. D. Batista, Phys. Rev. B **77**, 094406 (2008).
[4] Ch. Rüegg *et al.*, Nature (London) **423**, 62 (2003).
[5] M. B. Stone *et al.*, New J. Phys. **9**, 31 (2007).
[6] I. Affleck, Phys. Rev. B **41**, 6697 (1990); T. Giamarchi and A. M. Tsvelik, Phys. Rev. B **59**, 11 398 (1999).
[7] T. Nikuni *et al.*, Phys. Rev. Lett. **84**, 5868 (2000).
[8] M. Uchida *et al.*, J. Phys. Soc. Jpn. **70**, 1790 (2001).
[9] E. C. Samulon *et al.*, arXiv:0803.3830v1.
[10] M. Uchida *et al.*, Phys. Rev. B **66**, 054429 (2002).
[11] H. Tsujii *et al.*, Phys. Rev. B **72**, 214434 (2005).
[12] B. Xu *et al.*, Phys. Rev. B **77**, 014401 (2008).
[13] M. B. Stone *et al.*, Phys. Rev. B **77**, 134406 (2008).
[14] S. Hill *et al.* (private communication).
[15] In the absence of an *a priori* calculation of the Mn^{5+} magnetic form factor, we use the calculated Mn^{4+} magnetic form factor as a reasonable approximation.
[16] P. J. Brown, in *International Tables for Crystallography*, edited by A. J. C. Wilson (Kluwer Academic, London, 1995), Vol. C.
[17] H. J. Mattausch and H. K. Müller-Buschbaum, Z. Naturforsch., B **27**, 739 (1972).
[18] T. Nakajima *et al.*, J. Phys. Soc. Jpn. **75**, 054706 (2006).
[19] H.-J. Koo *et al.*, Inorg. Chem. **45**, 10 743 (2006).
[20] A. A. Aczel *et al.*, Acta Crystallogr. Sect. E **63**, i196 (2007); A. A. Aczel *et al.*, J. Cryst. Growth **310**, 870 (2008).
[21] E. Cuno and H. K. Müller-Buschbaum, Z. Anorg. Allg. Chem. **572**, 95 (1989).
[22] Y. Singh and D. C. Johnston, Phys. Rev. B **76**, 012407 (2007).
[23] M. T. Weller and S. J. Skinner, Acta Crystallogr. Sect. C **55**, 154 (1999).